

# Elucidating ion capture and transport mechanisms of Preyssler anions in aqueous solutions using biased MACE-accelerated MD simulations

Cite as: J. Chem. Phys. 163, 064502 (2025); doi: 10.1063/5.0279071

Submitted: 5 May 2025 • Accepted: 24 July 2025 •

Published Online: 12 August 2025



View Online



Export Citation



CrossMark

Quadri O. Adewuyi,<sup>1</sup> Suchona Akter,<sup>1</sup> Md Omar Faruque,<sup>1</sup> Dil K. Limbu,<sup>1</sup> Zhonghua Peng,<sup>1,a</sup> Praveen K. Thallapally,<sup>2,b</sup> and Mohammad R. Momeni<sup>1,c</sup>

## AFFILIATIONS

<sup>1</sup> Division of Energy, Matter and Systems, School of Science and Engineering, University of Missouri–Kansas City, Kansas City, Missouri 64110, USA

<sup>2</sup> Pacific Northwest National Laboratory, Richland, Washington 99352, USA

**Note:** This paper is part of the Special Topic, Chemical physics of ionic transport in solvents, polymers, and near interfaces.

a) **Electronic mail:** pengz@umkc.edu

b) **Electronic mail:** praveen.thallapally@pnnl.gov

c) **Author to whom correspondence should be addressed:** mmomenitaheri@umkc.edu

## ABSTRACT

Equilibrium and biased multi-atomic cluster expansion (MACE) accelerated molecular dynamics (MD) simulations in aqueous solutions are performed to investigate the ion capture and transport mechanisms of the  $\{P_5W_{30}\}$  Preyssler anion (PA) as the smallest representative member of the extended polyoxometalate (POM) family with an internal cavity. The unique interatomic interactions present in the internal cavity vs the exterior of PA are carefully investigated using equilibrium MACE MD simulations for two representative  $Na(H_2O)@PA$  and  $Na@PA$  complexes in aqueous solutions. Our careful analyses of radial distribution functions and coordination numbers show that the presence of confined water in  $Na(H_2O)@PA$  has profound modulating effects on the nature of the interactions of the encapsulated ion with the oxygens of the PA cavity. Using well-converged MACE-accelerated multiple walker well-tempered metadynamics simulations with nanosecond timescales, two different associative (ion exchange) and dissociative (ion ejection) ion transport mechanisms were carefully investigated for  $Na^+$  as one of the most abundant and representative ions present in seawater and saline solutions. By comparing systems with and without confined water, it was found that the presence of only one pre-encapsulated confined water in  $Na(H_2O)@PA$  dramatically changes the free energy landscape of ion transport processes. It was also found that the contraction and dilation of the two windows present in PA directly influence the  $Na^+$  and  $H_2O$  transport. The results from this work are helpful, as they show a viable path toward tuning the ion exchange and transport phenomena in aqueous solutions of POM molecular clusters and frameworks.

Published under an exclusive license by AIP Publishing. <https://doi.org/10.1063/5.0279071>

12 August 2025 13:48:15

## I. INTRODUCTION

Critical metals, including lithium, nickel, cobalt, and manganese, essential for advanced manufacturing and low-carbon technologies, are becoming scarce in land sources but abundant in saline solutions.<sup>1,2</sup> This has made extraction from aqueous sources such as saltwater and brine an intriguing research field, largely due to its significant impact on national economic development

and as a promising alternative to hard rock mining with lower environmental impacts.<sup>3,4</sup> Many saline brine solutions contain substantial amounts of critical metals, which could become pollutants if not properly managed but are valuable commodities when recovered. However, extracting these metals from saline sources presents significant challenges due to their low concentrations and the need for selective separation.<sup>5,6</sup> Current extraction methods include precipitation, ion exchange, solvent extraction, sorption, and

membrane-based technologies.<sup>4,6</sup> While conventional desalination membranes lack selectivity, emerging sub-nanostructured membranes and sorption technologies offer efficiency, scalability, and low costs, particularly for environmental remediation and selective metal recovery.<sup>5,7,8</sup>

Contemporary adsorbents recently employed for aqueous critical metal recovery include porous organic cages,<sup>9,10</sup> metal-organic frameworks (MOFs),<sup>11,12</sup> covalent-organic frameworks (COFs),<sup>13–15</sup> and porous polyoxometalate frameworks (POMFs),<sup>10,16</sup> to name a few. Despite advances in sorbent materials, challenges remain, including low selectivity, capacity, adsorption/desorption rates, and low recovery. These issues arise from the difficulty of selectively adsorbing trace metal ions in complex solutions with higher concentrations of competing ions, as well as a limited understanding of the molecular-level mechanisms driving the adsorption/desorption.

This work aims to provide a mechanistic molecular-level understanding of the adsorption and release of  $\text{Na}^+$  ions as the most abundant species commonly found in aqueous saline and brine solutions using robust, all-inorganic polyoxometalate (POM) molecular clusters. Redox-active POMs are nanosized anionic metal oxides of early transition metals. They can effectively transport protons by dispersing negative charges across the surface oxygen atoms, lowering their effective surface charge density.<sup>17–19</sup> Their high thermal stability, flexible binding modes, and stability over a wide pH range of 1–10 make POMs ideal candidates for selective adsorptive separation in harsh aqueous environments.<sup>20–22</sup> Specifically, the phosphotungstate Preyssler anion (PA,  $[\text{X}^{n+}\text{P}_5\text{W}_{30}\text{O}_{110}]^{(15-n)-}$  with X = metal ions) with a porous doughnut-shaped structure as the smallest member of the extended POM family with an internal cavity of  $\approx 5 \text{ \AA}$ <sup>20,23–26</sup> is an ideal sorbent for selectively adsorbing (mono-)hydrated metal ions of radius  $\approx 4 \text{ \AA}$  (Fig. 1).

PA has been experimentally shown to encapsulate potassium<sup>27,28</sup> and sodium<sup>29</sup> ions in its central cavity. Composed

of five  $\text{PW}_6$  units, each consisting of two groups of three corner-sharing  $\text{WO}_6$  octahedra, PA has an ellipsoid shape and an internal fivefold symmetry axis, with its doughnut shape believed to facilitate ion adsorption/desorption from aqueous solutions. Interestingly, the encapsulated metal ion is shown to significantly affect the POM's charge density, redox behavior, and basicity.<sup>26,30–38</sup> Examples of experimentally reported encapsulated ions include  $\text{Na}^+$ ,<sup>24,25,30</sup>  $\text{K}^+$ ,<sup>27,39,40</sup>  $\text{Ag}^+$ ,<sup>41–43</sup> lanthanides,<sup>30,31,36,38,44,45</sup>  $\text{Ca}^{2+}$ ,<sup>25,30,38</sup>  $\text{Bi}^{3+}$ ,<sup>30,38,46</sup>  $\text{Y}^{3+}$ ,<sup>25,30,38</sup> and actinides.<sup>25,30,36,44,47</sup>

While the extended family of POMs has been extensively studied for catalytic applications,<sup>48–53</sup> their structure–property relationships as sorbents for different critical metal capture and separation in aqueous solutions remain underexplored. This work addresses this knowledge gap by providing an in-depth exploration of ion capture and transport mechanisms in aqueous solutions of PA using equilibrium and well-tempered metadynamics (WT-MetaD) simulations enabled by accurate multiatomic cluster expansion (MACE)<sup>54,55</sup> foundation models. The accuracy of atomistic simulations relies on capturing interatomic interactions with high accuracy. While classical force fields are efficient for large-scale simulations, they often lack accuracy, have limited transferability, and are nonreactive by construction (with the exception of ReaxFF).<sup>56–60</sup> *Ab initio* molecular dynamics (AIMD) simulations improve accuracy by calculating forces on-the-fly via accurate electronic structure methods but suffer from limited length/time scales due to their high computational cost. Recently, machine learning interatomic potentials (MLIPs) have emerged as a promising alternative, providing a balance between accuracy and efficiency.<sup>54,61–75</sup> MACE-MLIPs, trained on extended datasets of material properties, bypass the cost of *ab initio* methods, enabling large-scale simulations with excellent performance for diverse applications.<sup>65–68</sup> This study utilizes MACE foundation models for both equilibrium and biased WT-MetaD simulations to investigate the capture and transport mechanisms of the targeted hydrated ions and PA. Two different “associative” (ion exchange) and “dissociative” (ion ejection) mechanisms are carefully investigated, with the effects of the presence of confined water in the PA cavity analyzed. This work is structured as follows. Section II provides theory and simulation details. The results and discussion are provided in Sec. III. Finally, conclusions and future outlooks are provided in Sec. IV.

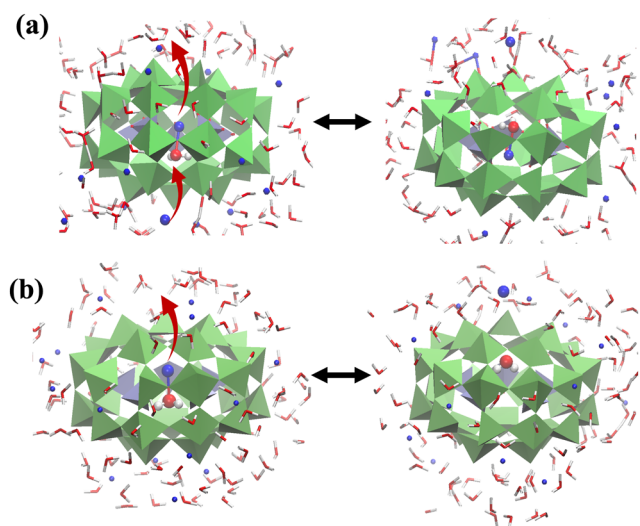


FIG. 1. Ion release mechanisms via (a) associative (ion exchange) and (b) dissociative (ion ejection) pathways using Preyssler anion polyoxometalates in aqueous solutions. H: white, O: red,  $\text{Na}^+$ : blue,  $\text{PO}_4$ : ice blue, and  $\text{WO}_6$ : green.

## II. SIMULATION DETAILS

The adapted workflow combining electronic structure calculations, AIMD, and MACE MD simulations for studying ion transport in aqueous solutions of PA is shown in Fig. 2. The isolated PA is fully minimized and solvated with water and 15 ions using PACKMOL.<sup>76</sup> Both AIMD and MACE MD simulations involving simulated annealing, equilibrium MD simulations, and WT-MetaD simulations are then performed to explore the free-energy landscape of ion capture by incorporating thermal fluctuations and conformational entropy from MD simulations at room temperature. AIMD is used as a reference, while MACE MD, interfaced with ASE and PLUMED, is used for generating well-converged simulated data. The free energy surfaces (FESs) calculated using MACE MD are benchmarked against AIMD for validation. More details are provided below.

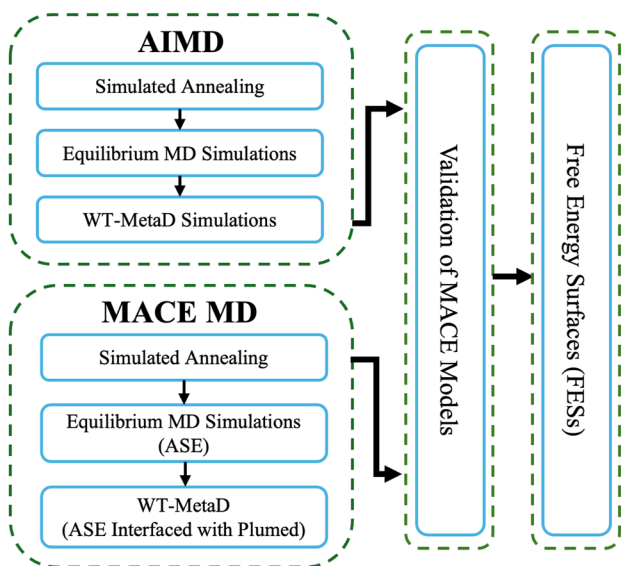


FIG. 2. Simulation workflow adapted in this work.

### A. Electronic structure calculations

All electronic structure calculations were performed using the revised PBE (revPBE)<sup>77</sup> functional within the periodic boundary conditions as implemented in the QUICKSTEP module of CP2K.<sup>78,79</sup> To account for van der Waals interactions, Grimme's D3 dispersion correction (revPBE-D3) with Becke-Johnson damping was employed.<sup>80,81</sup> The Kohn-Sham orbitals were expanded using the double- $\zeta$  valence with polarization Gaussian basis sets (DZVP-MOLOPT-SR-GTH), while core electrons were treated with the Goedecker-Teter-Hutter pseudopotentials optimized for PBE (GTH-PBE).<sup>82</sup> The self-consistent field convergence was set to  $10^{-5}$ . The simulation cell was prepared as follows: a single isolated PA cluster was extracted from the experimental crystal structure as obtained from Ref. 25 by removing solvent (water) molecules and ions. The cluster was then placed at the center of a cubic box with a Na-OH<sub>2</sub> molecule added to the center of its cavity, resulting in an overall stoichiometry of (Na(H<sub>2</sub>O)<sub>5</sub>W<sub>30</sub>O<sub>110</sub>)<sup>14-</sup> for the isolated Na(H<sub>2</sub>O)@PA system (see Fig. 1). The choice of addition of M-H<sub>2</sub>O (M = Na) to the cavity is motivated by the experimentally reported crystal structure of PA, which contains an encapsulated Na<sup>+</sup> ion bonded to a single water molecule inside its cavity.<sup>25</sup> First, a thorough benchmark of atomic positions and cell vectors was carried out without imposing any constraints. The structure was fully minimized at the revPBE-D3 level with plane-wave cutoffs ranging from 500 to 700 Ry, with/without effective Hubbard U corrections ( $U_{eff}$ )<sup>83</sup> for tungsten (W) and oxygen (O) atoms. The results of the benchmarks are provided in the supplementary material, Table S1. The obtained structural parameters were found to be marginally affected by variations in the details of the minimizations and were found to agree well with the experiment. The fully minimized Na(H<sub>2</sub>O)@PA structure with an energy cutoff of 700 Ry without ( $U_{eff}$ ) was used for MD simulations as explained in Sec. II B.

### B. AIMD simulations

To arrive at a neutral unit cell for PA containing Na(H<sub>2</sub>O)@PA, 14 Na<sup>+</sup> ions were randomly added using PACKMOL.<sup>76</sup> To model the aqueous solution, two different water contents were considered in this work, one with 109 and another with 149 water molecules randomly added to the exterior of PA, totaling 110 and 150 water molecules, respectively (see the supplementary material, Figs. S1 and S2). The lengths of the box were adjusted to achieve a density of 0.997 g/cm<sup>3</sup> for the liquid bulk water at room temperature, with lengths evaluated as  $l_{x,y,z} = 25.07$  and 25.65 Å for 110 and 150 water systems, respectively. For both water contents, three different plane-wave cutoffs of 300, 400, and 500 Ry were considered. To ensure proper randomizations, simulated annealing was performed in the canonical (NVT) ensemble at 700, 500, and 298 K, 2 ps each, totaling 6 ps for all considered systems. It is important to note that the finite number of water molecules considered here only allows for a partial solvation of the PA and free Na<sup>+</sup> ions, and simulating a fully bulk-like environment for them will necessitate many times more water molecules to be included in the simulation box. However, this would impose considerable computational costs, even using MACE, making our AIMD reference equilibrium and WT-MetaD simulations intractable. Although this might limit the capability of our simulations to capture the fully solvated states for both free ions and the encapsulated ion once released from the PA cavity, we believe that our simulated FESs have reasonable accuracy for the encapsulated and released states of the ion.

A timestep of 1 fs was employed using the CSVR thermostat<sup>84</sup> with a 20 fs time constant. Final snapshots from the 298 K simulated annealing stage were used to perform simulations in the NVT ensemble for 10 ps at 298 K for each system. The first 8 ps were discarded as equilibration, with the last 2 ps used for statistical analyses. Periodic boundary conditions were employed throughout, except during the initial optimization of the single isolated PA. To confirm that 2 ps is sufficient for reliable statistical analysis, our AIMD reference simulation was extended to 15 ps. After discarding the initial 8 ps, the remaining 7 ps was used for calculating RDFs, the results of which were consistent with those from the 10 ps simulation (see the supplementary material, Fig. S3). Considering the agreements between calculated radial distribution functions (RDFs) and the cost of on-the-fly AIMD simulations (supplementary material, Figs. S1 and S2), the smaller plane wave cutoff of 300 Ry with a REL-CUTOFF of 50 Ry was employed for 5 walker AIMD WT-MetaD simulations using the smaller 110 water system; more details are provided in Secs. II C and II D.

### C. Benchmarking equilibrium MACE MD simulations

The rather large size of the considered solvated PA systems (>500 atoms) limits the application of on-the-fly AIMD simulations in calculating well-converged properties. MACE foundation models trained on large datasets of material properties provide an attractive alternative. Here, using the Atomic Simulation Environment (ASE) Python package,<sup>85</sup> MACE MD simulations were performed using the MACE-MPA-0\_medium model. This model was chosen for its accuracy, enabled by training on an expanded dataset.<sup>55</sup> First, using the 110 H<sub>2</sub>O system, simulated annealing was performed at 700, 500, and 298 K temperatures in the NVT ensemble for a total of 150 ps, with 50 ps at each temperature. A timestep of 1 fs was used,

and a Langevin thermostat with a friction coefficient of  $0.1 \text{ ps}^{-1}$  was applied; see the [supplementary material](#), Fig. S6, for a comparison between the Langevin and Nosé–Hoover chain thermostats. Final snapshots from the simulated annealing at 298 K were used as initial configurations for production simulations in the NVT ensemble, for a total of 1 ns at 298 K. In the production simulations, the first 800 ps were discarded as equilibration, and the last 200 ps were used for statistical analysis.

To assess the sensitivity of the simulated data to different MACE models, extensive benchmarks using MD simulations in the NVT ensemble were performed. All simulations were run for a duration of 200 ps at 298 K. The primary goal of these simulations was to evaluate the performance and accuracy of all available MACE foundation models for capturing interatomic interactions of the PA system in aqueous solutions. Six MACE models known for their efficiency and accuracy were chosen, including MACE-MPA-0\_medium, MACE-MP-0b\_medium, MACE-MP-0b2\_small, MACE-MP-0b2\_medium, MACE-MP-0b2\_large, and MACE-MP-0b3\_medium. Calculated RDFs were used to assess how well different MACE models are able to capture key features of the ion–water vs ion–PA interactions compared to the reference AIMD data (see the [supplementary material](#), Fig. S7). The intramolecular W–O<sub>PA</sub> (i.e., tungsten to oxygen in PA) RDFs from different MACE models are well aligned with one another and with AIMD. The three peaks represent W interactions with three distinct PA oxygen types, namely (i) terminal oxygen, which shows the shortest W–O<sub>PA</sub> distance of 1.75 Å in MACE vs 1.70 Å in AIMD; (ii) bridging oxygen peaks near ≈1.95 Å in both MACE and AIMD; and finally (iii) PO<sub>4</sub> templating anion oxygen peaks at around 2.3 Å in MACE, while AIMD shows a less pronounced peak around 2.4 Å.

All studied MACE models are able to capture the first solvation shell of Na–O<sub>PA</sub> but slightly overestimate the second peak. For O<sub>W</sub>–O<sub>W</sub> (oxygen of water) RDFs, both AIMD and MACE agree on peak positions, though MACE predicts slightly more structured water. MACE models accurately reproduce RDFs for Na–O<sub>W</sub>, O<sub>W</sub>–H<sub>W</sub>, H<sub>W</sub>–H<sub>W</sub>, and H<sub>W</sub>–O<sub>PA</sub> pairs ([supplementary material](#), Figs. S7 and S8). Based on these extensive benchmarks, the MACE-MPA-0\_medium model was selected and used throughout this work.

#### D. Multiple walker MACE well-tempered metadynamics simulations

Metadynamics is a well-established enhanced sampling technique that uses a set of predefined collective variables (CVs) represented by  $s = s(R)$  as a function of nuclear coordinates R to build a history-dependent bias potential  $V(s)$  against previously visited configurations.<sup>86–88</sup> This approach is commonly used for accelerating the sampling of rare events, allowing large energy barriers to be surmounted within a feasible simulation time scale. The FES can then be estimated from the added history-dependent bias potential in the form of Gaussian functions<sup>89</sup>

$$G(s, s_k) = \sum_{k=1}^n We^{-\frac{\|s-s_k\|^2}{2\sigma^2}}, \quad (1)$$

with  $W$  and  $\sigma$  corresponding to the height and width of the Gaussian, respectively. In this work, the well-tempered variation of metadynamics (WT-MetaD) coupled with the multiple-walkers

approach<sup>90</sup> is employed for all enhanced sampling simulations. In this approach, the height of the deposited Gaussian in Eq. (1) is decreased exponentially as the external bias potential is deposited periodically,<sup>91,92</sup>

$$V_n(s) = \sum_{k=1}^n G(s, s_k) e^{-\left[\frac{\beta}{\gamma-1} V_{k-1}(s_k)\right]}, \quad (2)$$

where  $\beta = \frac{1}{k_B T}$  is the reciprocal temperature, and  $\gamma > 1$  is the bias factor.

This method requires a careful selection of CVs that can effectively capture the desired reaction mechanism. As mentioned previously, we have considered two associative (ion exchange) and dissociative (ion ejection) mechanisms in this work (see [Fig. 1](#)). In the former associative mechanism, the captured ion is exchanged with another ion from the solution, while in the latter dissociative mechanism, the ion is ejected by simple heating without another ion entering. To explore the reaction pathway for the associative mechanism, two continuous coordination number (CN) based CVs were employed, each defined by the general expression in the following equation:

$$S = \sum_{i,j} \left\{ \frac{1 - \left(\frac{r_{ij}}{r_c}\right)^8}{1 - \left(\frac{r_{ij}}{r_c}\right)^{16}} \right\}, \quad (3)$$

where  $r_{ij}$  is the distance between atoms  $i$  and  $j$  and  $r_c$  is the cutoff distance. For the associative mechanism, the first CV ( $S_1$ ) tracks the coordination between the encapsulated Na<sup>+</sup> ion and free H<sub>2</sub>O molecules at the exterior of the PA, with  $r_c$  set to 3.0 Å, while the second CV ( $S_2$ ) corresponds to the coordination between free Na<sup>+</sup> ions at the exterior of the cavity and the oxygen atoms of the PO<sub>4</sub> units, with an  $r_c$  of 3.2 Å. The cutoff distance  $r_c$  and the switching functions were fitted based on the first solvation shell peaks from the RDF analyses of the final 200 ps of the equilibrium MACE MD simulations (see the [supplementary material](#), Fig. S12 and Table S2). As mentioned, these CVs allow tracking the simultaneous transport of an encapsulated Na<sup>+</sup> ion out of the PA cavity and the adsorption of a free Na<sup>+</sup> ion from the solution, enabling the estimation of the overall free energy barrier for this ion exchange process.

Similarly, to explore the reaction pathway for the considered dissociative mechanism, two CN-based CVs were selected [Eq. (3)].  $S_1$  tracks the coordination between the encapsulated Na<sup>+</sup> ion and the oxygens of the PO<sub>4</sub> units with the  $r_c$  set to 3.2 Å, while  $S_2$  corresponds to the coordination between the encapsulated Na<sup>+</sup> ion and free H<sub>2</sub>O molecules at the exterior of the PA, with the  $r_c$  set to 3.0 Å (see the [supplementary material](#), Fig. S12). The two selected CVs enable analysis of the encapsulated Na<sup>+</sup> ion transport from the PA cavity to the aqueous solution by estimating its corresponding free energy barrier. All multiple walker WT-MetaD simulations were performed using the benchmarked MACE-MPA-0\_medium model. Gaussian hills (1 kJ/mol height and 0.5 Å width) were added every 500 MD steps. The bias factor, which governs the rate at which the Gaussian height decays over time, was set to 15. These parameters were selected following necessary benchmarks of the Gaussian height and bias factor (see the [supplementary material](#), Figs. S18 and S19), in accordance with the standard protocol established by Ref. 91 and supported by parameter recommendations

**TABLE I.** Equilibrium MACE MD calculated RDFs ( $R$  in Å) and average CNs for  $\text{Na}(\text{H}_2\text{O})@\text{PA}$  and  $\text{Na}@\text{PA}$  systems. Interior refers to the interactions inside the PA cavity, while exterior corresponds to the interactions at the periphery of PA in aqueous solution. See the text for more details.

System	Pair	$\text{Na}(\text{H}_2\text{O})@\text{PA}$		$\text{Na}@\text{PA}$	
		$R$ (Å)	CN (Avg.)	$R$ (Å)	CN (Avg.)
Interior	$\text{Na}-\text{O}_{\text{PO}_4}$	2.63	$4.89 \pm 0.32$	2.73	$6.46 \pm 0.58$
	$\text{Na}-\text{O}_W$	2.30	$0.77 \pm 0.12$	...	...
	$\text{H}_W-\text{O}_{\text{PO}_4}$	1.81	$3.55 \pm 0.23$	...	...
Exterior	$\text{H}_W-\text{O}_{\text{Term}}$	1.79	$1.41 \pm 0.02$	1.82	$0.99 \pm 0.04$
	$\text{H}_W-\text{O}_{\text{Bridg}}$	1.91	$0.16 \pm 0.05$	1.91	$0.09 \pm 0.02$
	$\text{Na}-\text{O}_{\text{Term}}$	2.32	$1.48 \pm 0.09$	2.35	$1.61 \pm 0.06$
	$\text{Na}-\text{O}_{\text{Bridg}}$	2.51	$1.28 \pm 0.13$	2.75	$0.99 \pm 0.04$
	$\text{Na}-\text{O}_W$	2.38	$2.86 \pm 0.12$	2.35	$2.38 \pm 0.13$

from Refs. 93–95. Benchmark tests demonstrated that barrier estimates remained consistent (within 0.7 kcal/mol) across variations in bias factor and Gaussian height, indicating robustness of the chosen parameters and reliability of the estimated FESs. All WT-MetaD

simulations for MACE were performed using ASE<sup>85</sup> interfaced with PLUMED.<sup>96,97</sup> Five walkers were used for all MACE simulations, each run for 250 ps, totaling 1.25 ns of simulation time.

For further validation, representative WT-MetaD runs were also performed at the reference rev-PBE-D3 level for the  $\text{Na}(\text{H}_2\text{O})@\text{PA}$  system using CP2K interfaced with PLUMED's multiple-walker algorithm.<sup>96,97</sup> The bias factor and Gaussian width and height parameters were kept the same as in the MACE simulations. Due to AIMD's high cost, each walker was run for 15 ps, totaling 75 ps across five walkers, with Gaussians added every 40 MD steps. These benchmarks were performed for ejecting the  $\text{Na}^+$  ion through the considered dissociative mechanism for the  $\text{Na}(\text{H}_2\text{O})@\text{PA}$  system, which resulted in a similar free energy barrier (supplementary material, Figs. S4 and S5). Finally, the pywindow package<sup>98</sup> was used to evaluate fluctuations of the PA windows during ion transit.

### III. RESULTS AND DISCUSSION

To understand the ion capture and transport mechanism of the representative  $\text{Na}^+$  ion in aqueous PA solutions, equilibrium and biased MD simulations were carried out using the validated MACE-MPA-0\_medium model, benchmarked against AIMD. Our initial

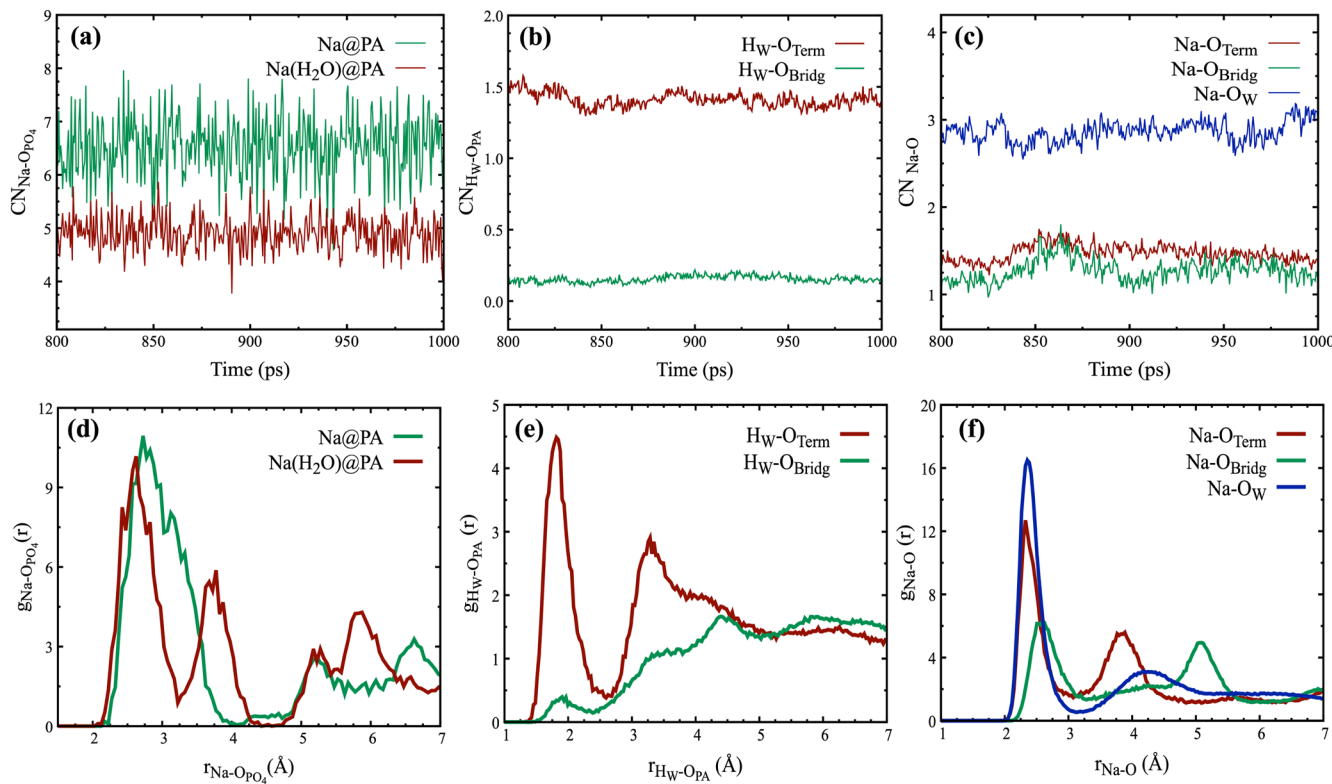


**FIG. 3.** (Top row) Equilibrium MACE MD simulated time evolution of the CNs for (a) the encapsulated  $\text{Na}^+-\text{O}_{\text{PO}_4}$  interactions in  $\text{Na}@\text{PA}$  (green) and  $\text{Na}(\text{H}_2\text{O})@\text{PA}$  (brown) (b) hydrogen of the free water molecules ( $H_W$ ) to the terminal (brown) and bridging (green) oxygens of the PA in  $\text{Na}(\text{H}_2\text{O})@\text{PA}$  and (c) the free  $\text{Na}^+$  ions to the terminal (brown) and bridging (green) oxygens of the PA in  $\text{Na}(\text{H}_2\text{O})@\text{PA}$  as well as water molecules (blue). The bottom panels (d–f) show the corresponding RDFs. Other plots for the  $\text{Na}@\text{PA}$  system are given in the supplementary material, Fig. S9. See the text for more details.

analyses focus on equilibrium properties with biased MACE MD simulated results for the two considered mechanisms discussed in Sec. III B.

### A. Equilibrium MACE MD simulations

The coordination environments of  $\text{Na}^+$  ions in the Na@PA and  $\text{Na}(\text{H}_2\text{O})@\text{PA}$  systems are investigated using average CNs and RDFs for the first solvation shells, extracted from equilibrium MACE MD simulations (see Table I and Fig. 3). The nature of interactions within the interior of the PA cavity compared to its exterior is discussed separately below.

#### 1. Interior interactions

The encapsulated  $\text{Na}^+$  ion in  $\text{Na}(\text{H}_2\text{O})@\text{PA}$  is coordinated to a confined water molecule on one side and interacts with an average of  $4.89 \pm 0.32$  oxygens of the  $\text{PO}_4$  templating anions from the other side [see Table I and Fig. 3(a)]. The calculated  $\text{Na}-\text{O}_{\text{PO}_4}$  CN from MACE MD equilibrium simulations for  $\text{Na}(\text{H}_2\text{O})@\text{PA}$  shows minor fluctuations over time [Fig. 3(a)]. The calculated RDFs for the  $\text{Na}-\text{O}_{\text{PO}_4}$  pair show two sharp peaks at  $\approx 2.65 \text{ \AA}$  and  $\approx 3.75 \text{ \AA}$  [Fig. 3(d)], with the first peak arising from interactions with the  $\text{PO}_4$  oxygens on the same side as  $\text{Na}^+$  and the second from those on the opposite, water-facing side.

In comparison, the average CN for the same  $\text{Na}-\text{O}_{\text{PO}_4}$  pair in the Na@PA system (i.e., the system without confined water) increases significantly to  $6.46 \pm 0.58$  [Table I and Fig. 3(a)], indicating that  $\text{Na}^+$  can access more  $\text{PO}_4$  oxygens inside the cavity at 298 K. The calculated  $\text{Na}-\text{O}_{\text{PO}_4}$  RDF shown in Fig. 3(d) also gives a broad peak at  $\approx 2.75 \text{ \AA}$  for the first solvation shell. This is simply because in  $\text{Na}(\text{H}_2\text{O})@\text{PA}$ , the confined water molecule limits  $\text{Na}^+$  interactions with  $\text{PO}_4$  oxygens on the water-facing side, reducing its overall coordination. Interestingly, the average CN between the encapsulated  $\text{Na}^+$  and the confined water molecule in  $\text{Na}(\text{H}_2\text{O})@\text{PA}$  is less than 1 ( $0.77 \pm 0.12$ , Table I). This is likely due to the competition between  $\text{O}_W$  and  $\text{O}_{\text{PO}_4}$  atoms for coordination to the encapsulated  $\text{Na}^+$  ion. Meanwhile, hydrogens of the water molecule ( $\text{H}_W$ ) form strong hydrogen bonds (H-bonds) with the oxygens of  $\text{PO}_4$ , with an average CN of  $3.55 \pm 0.23$  and a first solvation shell distance of  $1.81 \text{ \AA}$  (Table I and supplementary material, Fig. S10). These H-bond interactions stabilize the  $\text{Na}(\text{H}_2\text{O})$  unit inside the cavity and shield  $\text{Na}^+$  ion from forming strong interactions with the  $\text{PO}_4$  templating anions from both sides of the cavity, as observed in Na@PA.

#### 2. Exterior interactions

On the exterior, PA can form H-bonds with bulk water through its terminal and bridging oxygens and/or adsorb free  $\text{Na}^+$  ions. In agreement with Ref. 99, the H-bonds formed between the water molecule and the more accessible terminal oxygens ( $\text{H}_W-\text{O}_{\text{Term}}$ ) in both  $\text{Na}(\text{H}_2\text{O})@\text{PA}$  and Na@PA systems are stronger than those of the bridging oxygens (see Table I). The average CNs are slightly higher for the  $\text{Na}(\text{H}_2\text{O})@\text{PA}$  than for Na@PA ( $1.41 \pm 0.02$  vs  $0.99 \pm 0.04$ ). Calculated RDFs also show stronger  $\text{H}_W-\text{O}_{\text{Term}}$  H-bonds ( $\approx 1.79-1.82 \text{ \AA}$ ) compared to  $\text{H}_W-\text{O}_{\text{Bridg}}$  H-bonds ( $\approx 1.91 \text{ \AA}$ ) [see Table I and Fig. 3(e)].

For  $\text{Na}^+$  interactions with the terminal and bridging oxygens of the  $\text{Na}(\text{H}_2\text{O})@\text{PA}$  and Na@PA systems, the average bond lengths for  $\text{Na}^+-\text{O}_{\text{Term}}$  are found to be similar ( $2.32$  and  $2.35 \text{ \AA}$ ), while the  $\text{Na}^+-\text{O}_{\text{Bridg}}$  bonds are significantly shorter in  $\text{Na}(\text{H}_2\text{O})@\text{PA}$  than

Na@PA ( $2.51$  vs  $2.75 \text{ \AA}$ , Table I). The calculated CNs show that, like  $\text{H}_W-\text{O}_{\text{PA}}$  interactions,  $\text{Na}^+$  forms slightly stronger coordination bonds with the more accessible terminal oxygens than the bridging ones. Both  $\text{Na}(\text{H}_2\text{O})@\text{PA}$  and Na@PA systems show rather similar free  $\text{Na}^+$  to  $\text{O}_W$  interactions, with average CNs of  $2.86 \pm 0.12$  and  $2.38 \pm 0.13$ . Considering the well-established CN of 5-6 for a fully solvated  $\text{Na}^+$  ion in bulk solutions, our calculated data show a partial solvation for the free  $\text{Na}^+$  ions. One possible explanation is that the PA oxygens are competing with water molecules to interact with the free  $\text{Na}^+$  ions. Specifically, considering the interactions of free  $\text{Na}^+$  ions with both oxygens of water and PA combined, one arrives at CNs of 5.62 in  $\text{Na}(\text{H}_2\text{O})@\text{PA}$  and 4.98 in Na@PA (Table I). These values are comparable to the known CN of 5-6 for  $\text{Na}^+$  ions in bulk water, as mentioned earlier. However, the low calculated CNs for  $\text{Na}^+$  ions and free water molecules could also be an artifact of using a limited number of  $\text{H}_2\text{O}$  molecules, which only allows for a partial solvation of the free  $\text{Na}^+$  ions. To verify this, many more water molecules will be needed to form complete solvation shells around PA in order to properly solvate and shield it from the free  $\text{Na}^+$  ions. However, as mentioned previously, this would make our simulations intractable, especially for the reference AIMD simulations, and is not undertaken in this work. The calculated  $\text{Na}-\text{O}_W$  distances are  $2.38 \text{ \AA}$  and  $2.35 \text{ \AA}$  for the  $\text{Na}(\text{H}_2\text{O})@\text{PA}$  and Na@PA systems, respectively. In contrast, the  $\text{Na}-\text{O}_W$  distance for the confined water in  $\text{Na}(\text{H}_2\text{O})@\text{PA}$  is slightly shorter ( $2.30 \text{ \AA}$ ). This shorter distance may indicate stronger hydrogen bonding interactions between confined water and  $\text{O}_{\text{PO}_4}$ . These hydrogen bonds reduce the mobility of the water molecule, allowing the encapsulated  $\text{Na}^+$  ion to maintain closer contact with the confined water without the interference of other water molecules.

Altogether, our detailed analyses show that with 109 water molecules present in the simulation box, free  $\text{Na}^+$  ions are rather similarly solvated by both free water and terminal oxygens of PA [see Table I and Fig. 3(f)]. Interestingly, the confined water in  $\text{Na}(\text{H}_2\text{O})@\text{PA}$  is indirectly influencing PA interactions with the environment (Table I and Fig. 3, and supplementary material, Fig. S9). Over the total time of 1 ns, the encapsulated  $\text{Na}^+$  ion was found to remain stable within the cavity, suggesting that the ion capture and transport is a rare event at 298 K. Therefore, to further investigate this, biased MACE MD simulations were performed, the results of which are discussed below.

### B. WT-MetaD simulations for ion vs water transport

Using biased MACE MD simulations, two transport mechanisms are explored in this work, including the “associative” and “dissociative” pathways. In the associative mechanism, an ion exchange occurs where a free  $\text{Na}^+$  ion from the aqueous solution enters the cavity from the water window, with the already encapsulated ion exiting from the opposite side. In the dissociative mechanism, the encapsulated ion exits without another ion entering. In both cases, the confined water remains inside the cavity. Structural and energetic details are discussed below.

#### 1. Associative mechanism for ion transport

In the initial configuration for the first metastable state (MS1), the  $\text{Na}^+$  ion in  $\text{Na}(\text{H}_2\text{O})@\text{PA}$  resides in the side cavity of PA and is coordinated to the confined  $\text{H}_2\text{O}$  molecule as illustrated at the

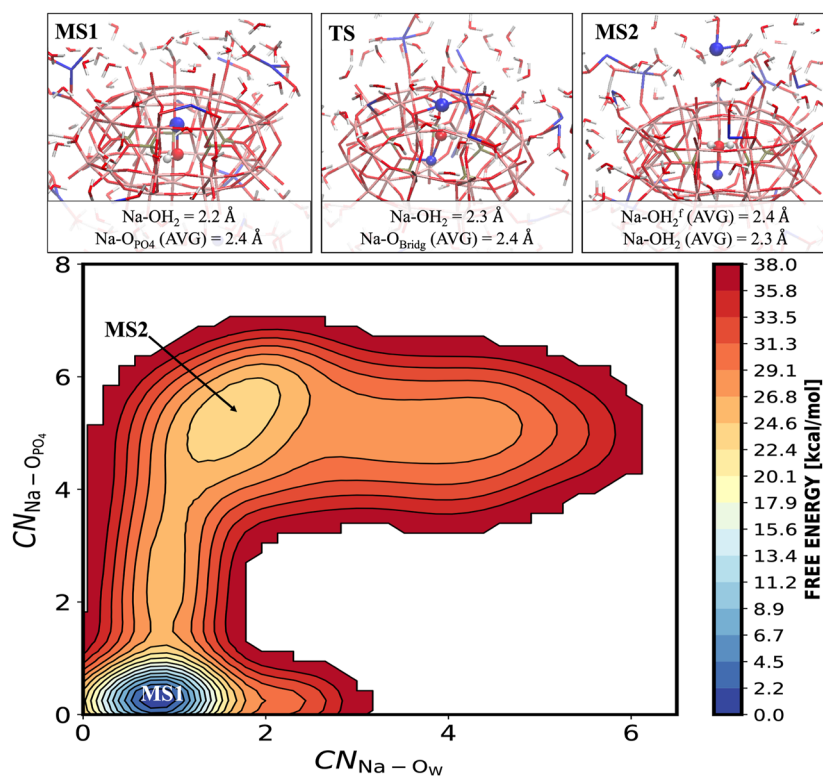


**FIG. 4.** MACE WT-MetaD calculated FES (in kcal/mol) for ion transport through the associative mechanism. Representative snapshots for MS1, TS, and MS2 states are also given, with the main geometric parameters shown. See the text for more details.

top of Fig. 4. Equilibrium MD analysis showed strong electrostatic interactions between Na<sup>+</sup> and oxygens of PO<sub>4</sub> (O<sub>PO4</sub>) on one side, while the confined water forms hydrogen bonds with O<sub>PO4</sub> from the other side. As mentioned, in the associative mechanism, a Na<sup>+</sup> ion from solution is encapsulated, followed by the ejection of the already encapsulated one. As mentioned, this ion exchange process is simulated using two CVs: (i) CN between the encapsulated Na<sup>+</sup> ion and the surrounding water oxygens, CN<sub>Na - O<sub>W</sub></sub>, and (ii) CN between the free Na<sup>+</sup> ions and O<sub>PO4</sub>, i.e., CN<sub>Na<sup>+</sup> - O<sub>PO4</sub></sub>.

A detailed analysis of the trajectory reveals that, as the reaction proceeds, exterior Na<sup>+</sup> ions approach the cavity by first interacting with the terminal oxygens of PA, while the initially encapsulated Na<sup>+</sup> remains stable inside. One of the Na<sup>+</sup> ions eventually enters through the water-facing window, forming a solvent-separated ion pair-like intermediate species, where both Na<sup>+</sup> ions strongly interact with the confined H<sub>2</sub>O (see Fig. 4). The initially encapsulated Na<sup>+</sup> ion is then ejected into the solution. The calculated FES shows the lowest energy basin at MS1, where the initial Na<sup>+</sup> is solely coordinated to the confined water, with CN<sub>Na - O<sub>W</sub></sub> = 0.92 ± 0.04 and CN<sub>Na<sup>+</sup> - O<sub>PO4</sub></sub> = 0.19 ± 0.14 (see Fig. 4 and Table II).

The transition state (TS) is characterized by CN<sub>Na - O<sub>W</sub></sub> fluctuating around 1 and CN<sub>Na<sup>+</sup> - O<sub>PO4</sub></sub> increasing to ≈2-3, with average calculated CNs of 0.91 ± 0.06 and 2.87 ± 0.83 (see Table II). This indicates that the original Na<sup>+</sup> remains inside the cavity while a free Na<sup>+</sup> enters and coordinates with ≈3 oxygen atoms of the PO<sub>4</sub> units. The free energy barrier for this considered associative mechanism

**TABLE II.** MACE WT-MetaD calculated changes in the free energies ( $\Delta F$ ) and average CNs for the Na(H<sub>2</sub>O)@PA and Na@PA systems considering the associative (Ass.) and dissociative (Dis.) mechanisms. For the Na<sup>+</sup> ion, both the associative (Ass. Na<sup>+</sup>) and dissociative (Dis. Na<sup>+</sup>) mechanisms are considered in Na(H<sub>2</sub>O)@PA, while the data are tabulated for the dissociative mechanism in Na@PA. Data for ejecting confined water in Na(H<sub>2</sub>O)@PA through the dissociative mechanism are also shown (Dis. H<sub>2</sub>O). The superscripts and subscripts in TS show the changes (rounded to whole numbers) in CNs for CV1 and CV2, respectively. See the text for more details.

Na(H <sub>2</sub> O)@PA			
System	$\Delta F$ (kcal/mol)	CN1 (Avg.)	CN2 (Avg.)
Ass. Na <sup>+</sup>	<b>MS1</b>	0	0.92 ± 0.04
	TS <sub>0→6</sub> <sup>1→2</sup>	26.8	0.91 ± 0.06
	<b>MS2</b>	24.6	1.87 ± 0.22
Dis. Na <sup>+</sup>	<b>MS1</b>	0	4.89 ± 0.55
	TS <sub>1→2</sub> <sup>5→0</sup>	21.3	0.47 ± 0.13
	<b>MS2</b>	19.2	0.38 ± 0.07
Dis. H <sub>2</sub> O	<b>MS1</b>	0	4.62 ± 0.44
	TS <sub>2→6</sub> <sup>5→0</sup>	25.6	1.21 ± 0.20
	<b>MS2</b>	19.2	0.01 ± 0.01
Na@PA			
Dis. Na <sup>+</sup>	<b>MS1</b>	0	5.76 ± 0.46
	TS <sub>0→3</sub> <sup>6→0</sup>	23.5	1.30 ± 0.49
	<b>MS2</b>	17.1	0.05 ± 0.05

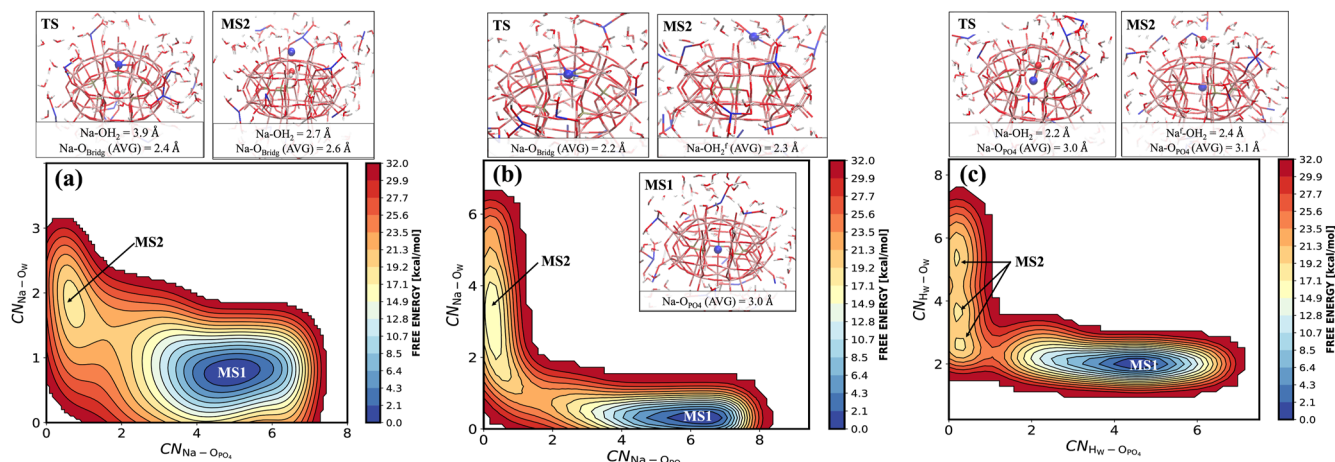


**FIG. 5.** Calculated FESs (in kcal/mol) for the dissociative mechanism involving  $\text{Na}^+$  ion in (a)  $\text{Na}(\text{H}_2\text{O})@\text{PA}$  and (b)  $\text{Na}@\text{PA}$  systems. Panel (c) shows the calculated FES for ejecting the confined water in  $\text{Na}(\text{H}_2\text{O})@\text{PA}$ . Representative snapshots for MS1, TS, and MS2 states are also given, with the main geometric parameters shown. See the text for more details.

is calculated as 26.8 kcal/mol. After passing through the barrier, the system reaches the second metastable state (MS2) at 24.6 kcal/mol, where the encapsulated  $\text{Na}^+$  ion has fully exited the cavity. In MS2,  $\text{CN}_{\text{Na}-\text{O}_W}$  is  $\approx 2$ , and  $\text{CN}_{\text{Na}^+-\text{O}_{\text{PO}_4}}$  is  $\approx 5$ –6, with average values of  $1.87 \pm 0.22$  and  $5.30 \pm 0.46$ , respectively. This confirms that the pre-encapsulated  $\text{Na}^+$  ion exits the cavity and coordinates to the exterior water molecules, while the newly encapsulated  $\text{Na}^+$  ion is now strongly bonded to  $\text{O}_{\text{PO}_4}$ . These calculated CNs are close to those from equilibrium MACE MD simulations reported in Table I.

This rather high calculated energy barrier raises an important question: What would be the free energy barrier of ejecting a  $\text{Na}^+$  ion from the cavity in the absence of another incoming ion? In other words, can one eject the ion by simply heating the PA solution in deionized water? This question motivated us to further investigate an alternative “dissociative” pathway focusing on the structural and

free energy changes involved in releasing the encapsulated  $\text{Na}^+$  ion directly into the solution.

## 2. Dissociative mechanism for ion transport

The dissociative transport mechanisms were examined by defining two new CVs based on the CN of the encapsulated  $\text{Na}^+$  ion to (i)  $\text{O}_{\text{PO}_4}$  (i.e.,  $\text{CN}_{\text{Na}-\text{O}_{\text{PO}_4}}$ ) and (ii) oxygens of bulk water ( $\text{O}_W$ ) (i.e.,  $\text{CN}_{\text{Na}-\text{O}_W}$ ). The simulated FES for the  $\text{Na}(\text{H}_2\text{O})@\text{PA}$  system is shown in Fig. 5(a). The initial MS1 configuration is the same as that of the associative pathway. In the TS, the confined  $\text{Na}^+$  begins to detach from the water while concurrently interacting with both  $\text{O}_{\text{PO}_4}$  and the bridging oxygens ( $\text{O}_{\text{bridg}}$ ) of PA. In the TS, the calculated  $\text{CN}_{\text{Na}-\text{O}_{\text{PO}_4}}$  drops toward zero, while  $\text{CN}_{\text{Na}-\text{O}_W}$  rises to about 2. The average values,  $0.47 \pm 0.13$  and  $1.29 \pm 0.01$ , indicate that the encapsulated  $\text{Na}^+$  is detaching from the  $\text{O}_{\text{PO}_4}$  units and beginning to interact

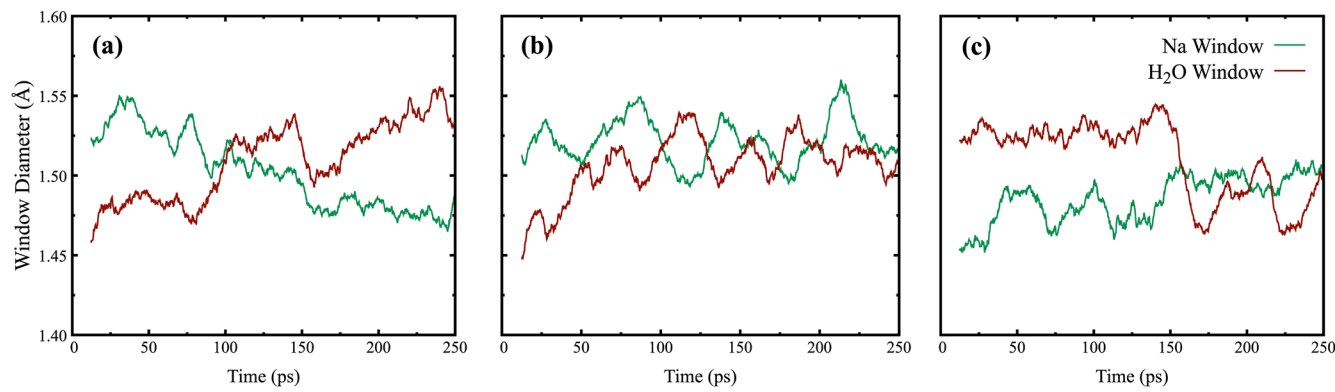


**FIG. 6.** MACE MD calculated time evolution of the PA window diameters during the considered (a) associative mechanism for  $\text{Na}(\text{H}_2\text{O})@\text{PA}$ , (b) dissociative mechanism for  $\text{Na}^+$  in  $\text{Na}(\text{H}_2\text{O})@\text{PA}$ , and (c) dissociative mechanism for ejecting water in  $\text{Na}(\text{H}_2\text{O})@\text{PA}$ .

with exterior water molecules (see Table II). The free energy barrier from MS1 to TS for this dissociative mechanism is estimated to be  $\approx 21.3$  kcal/mol. This value matches that of the free energy barrier obtained from reference AIMD simulations (see the supplementary material, Fig. S4). As expected, in MS2, with a calculated  $\Delta F$  of 19.2 kcal/mol,  $CN_{Na-O_{PO_4}}$  drops to zero while  $CN_{Na-O_W}$  rises to  $\approx 2$ . The average values,  $0.38 \pm 0.07$  and  $1.89 \pm 0.30$ , confirm the complete ejection of the  $Na^+$  into the solution, leaving the water molecule behind [Fig. 5(a)].

This calculated barrier is 5.5 kcal/mol lower than that of the associative mechanism discussed in Sec. III B 1. Analysis of the window diameters averaged across trajectories from all five walkers using the pywindow code<sup>98</sup> shows that the  $Na(H_2O)$  window contracts (expands) by  $\approx 0.1$  Å during ion entry and exit [see Fig. 6(a)]. In contrast, during the dissociative mechanism for the  $Na^+$  ion, the changes in the diameters of both windows are  $\approx 0.05$  Å, which is about half [see Fig. 5(b)]. We recognize that the implications of these results for ion capture using PA are rather significant, as they show that efficient ion capture and release by PA should be performed in two separate steps: (i) heating in deionized water to eject the already encapsulated ion followed by (ii) transferring the POM adsorbent to the target solution for the selective ion capture. We, however, caution against generalizing these results to other POMs with different windows and cavity sizes.

### 3. Effects of the presence of the confined water

As shown from our equilibrium MACE MD data, water coordination to the encapsulated ion inside the cavity has a significant impact on its interactions within PA. As such, water is expected to affect the calculated FESs for ion capture and transport in the  $Na(H_2O)@PA$  system. As mentioned previously, in  $Na(H_2O)@PA$ , the encapsulated  $Na^+$  ion is stabilized by interactions with both confined water and  $O_{PO_4}$ , with an average  $CN_{Na-O_{PO_4}}$  of  $4.89 \pm 0.32$  (see Table I). In contrast, in  $Na@PA$  (i.e., without confined water), the coordination increases to  $6.46 \pm 0.58$ . To assess the impact of confined water, the FES was calculated for the dissociative mechanism in  $Na@PA$  using the same two CVs as for  $Na(H_2O)@PA$  [Fig. 5(b)]. In MS1,  $CN_{Na-O_{PO_4}}$  and  $CN_{Na-O_W}$  are calculated to be  $5.76 \pm 0.46$  and  $0.02 \pm 0.00$ , respectively (Table II). At the TS, these change to  $1.30 \pm 0.49$  and  $0.35 \pm 0.20$ , indicating partial ejection of the  $Na^+$  ion from the cavity, though it still remains near the window and has not yet fully ejected into the solution.

The calculated free energy barrier in  $Na@PA$  is estimated to be  $\approx 23.5$  kcal/mol. In MS2 (17.1 kcal/mol), as expected,  $CN_{Na-O_{PO_4}}$  drops to near zero ( $0.05 \pm 0.05$ ), while  $CN_{Na-O_W}$  increases to  $2.79 \pm 0.57$ , confirming complete ion release into the aqueous solution. This barrier is around  $\approx 2.2$  kcal/mol higher than the  $Na(H_2O)@PA$  system. This can likely be attributed to water shielding  $Na^+$  from interacting with some of the  $O_{PO_4}$  sites, as seen from our equilibrium MACE MD data. Our RDF analyses [Fig. 3(d)] further showed that the confined water restricts ion mobility, pushing  $Na^+$  toward a side pocket in  $Na(H_2O)@PA$ . As mentioned, the calculated RDFs for  $Na-H_2O@PA$  reveal two distinct  $Na-O_{PO_4}$  peaks at  $\approx 2.75$  Å and  $\approx 3.75$  Å, showing asymmetric coordination due to water-induced ion displacement. In contrast,  $Na@PA$  showed a single broad peak, indicating a delocalized  $Na^+$  interacting with almost all 10  $O_{PO_4}$  sites. As such, the confined water's role is to weaken  $Na^+-O_{PO_4}$  interactions, reducing its CN and facilitating ion release,

as confirmed by both equilibrium and biased MD data. The ion must also break its bond with the confined water in order to freely diffuse into the solution. The lower energy cost of breaking a single  $Na-H_2O$  bond ( $CN_{Na-O_W} = 0.77 \pm 0.12$ ) compared to the drop in  $Na-O_{PO_4}$  coordination from  $6.46 \pm 0.58$ – $4.89 \pm 0.32$  (see Table I) helps offset this, explaining the small energy barrier difference. Overall, confined water is found to enhance ion mobility through lowering the free energy barrier to ion capture and release in PA. The role of water in shielding the ion from the oxygens of POMs is likely similar in other POM clusters and their extended frameworks and should be explicitly taken into account when studying transport in these intriguing systems.

### 4. Dissociative mechanism for water transport

As shown earlier, confined water weakens  $Na^+-O_{PO_4}$  interactions, lowering the free energy barrier by 2.2 kcal/mol. These prompted us to explore the FES for ejecting confined water itself. Two CVs were selected, based on the CN of the hydrogen atoms of the confined water ( $H_W$ ) to (i)  $O_{PO_4}$  (i.e.,  $CN_{H_W-O_{PO_4}}$ ) and (ii) oxygens of the bulk water (i.e.,  $CN_{H_W-O_W}$ ). In MS1, the confined water strongly interacts with the encapsulated  $Na^+$  ion and forms strong H-bonds with  $O_{PO_4}$  with an average CN of  $4.62 \pm 0.44$  (Table II), stabilizing itself within the cavity. At the TS,  $CN_{H_W-O_{PO_4}}$  drops to  $1.21 \pm 0.20$ , while  $CN_{H_W-O_W}$  rises to  $2.18 \pm 0.09$ , indicating partial dissociation from the oxygens of the templating anions. The free energy barrier for water ejection is  $\approx 25.6$  kcal/mol, which is 4.3 kcal/mol higher than that for  $Na^+$  in  $Na(H_2O)@PA$  [see Table II and Fig. 5(c)].

In MS2 at 19.2 kcal/mol,  $CN_{H_W-O_{PO_4}}$  drops to near zero, while  $CN_{H_W-O_W}$  rises to  $4.40 \pm 1.01$ . Interestingly, MS2 reveals three distinct minima with calculated  $CN_{H_W-O_W}$  values of  $\approx 2$  (still water is interacting with PA bridging oxygens),  $\approx 3$  (transitioning to out of the window), and  $\approx 5$  (full solvation in bulk aqueous environment). The calculated 2.1 kcal/mol energy barrier that separates these three minima shows that all of them should be accessible at room temperature. The higher calculated barrier of 4.3 kcal/mol for water ejection likely arises from its larger kinetic diameter ( $\approx 2.65$ ) compared to bare  $Na^+$  ( $\approx 2.02$  Å), making transport through the PA window more difficult. Figure 6(c) shows that, when ejecting water, the change in the calculated water window averaged over all five walkers is  $\approx 0.1$  Å, with the Na window staying more or less the same. This shows that upon heating the  $Na(H_2O)@PA$  system in deionized water,  $Na^+$  will likely be the first species that is going to be released into the solution before confined water can be ejected.

## IV. CONCLUSIONS

Using equilibrium and biased MACE MD simulations, carefully validated against reference AIMD data, we have studied the aqueous solution chemistry of the ion capture and transport mechanisms in PA as the smallest member of the extended POM family with a cavity large enough to host transition metal ions. Comparisons between  $Na(H_2O)@PA$  and  $Na@PA$  systems in aqueous solutions showed that confined water has a significant effect by shielding the encapsulated  $Na^+$  ion from interactions with oxygens of the  $PO_4$  templating anions. Through well-converged multiple-walker WT-MetaD simulations, two different associative and dissociative ion transport mechanisms were carefully investigated. Our detailed

analyses showed that the ion capture in PA occurs through a dissociative mechanism with a free energy barrier of 21.3 kcal/mol. The results obtained from this work demonstrate the critical role of internal hydration within the PA cavity in tuning ion exchange and transport processes, offering important insights into the dynamic behavior of ion capture and release in POMs. Our future experimental and theoretical studies will focus on exploring how encapsulated hydronium affects ion exchange and extending these studies to 2D and 3D frameworks of PA and similar POMs.

## SUPPLEMENTARY MATERIAL

The [supplementary material](#) contains details of structural parameters from geometry optimizations, radial distribution functions from both AIMD and MACE MD simulations, time evolution of coordination numbers from equilibrium simulations for Na@PA, schematic representations of collective variables (CVs), switching functions, and cutoff radius fittings, as well as the time evolution of CVs from MACE MD for all considered systems and the free energy surface plot calculated from reference AIMD, along with its corresponding time evolution of CVs.

## ACKNOWLEDGMENTS

This work was supported by the U.S. Department of Energy Office of Science, Basic Energy Sciences Program (Grant No. DE-SC0024512). P.K.T. acknowledges DOE Nuclear Energy–Materials Research and Waste Form Development Campaign. Particularly, P.K.T. acknowledges Dr. Ken Marsden (INL), Mrs. Amy Welty (INL), and Mrs. Kimberly Gray (DOE Nuclear Energy). Z.P. and M.R.M. acknowledge the UMKC Tier 1 Funding for Excellence grant for support. Simulations presented in this work used resources from Bridges-2 at Pittsburgh Supercomputing Center through allocations Grant Nos. PHY230099 and PHY240029P from the Advanced Cyberinfrastructure Coordination Ecosystem: Services & Support (ACCESS) program,<sup>100</sup> which is supported by National Science Foundation Grants Nos. 2138259, 2138286, 2138307, 2137603, and 2138296. Technical support and computing resources provided by the HPC Center at UMKC are also gratefully acknowledged.

## AUTHOR DECLARATIONS

### Conflict of Interest

The authors have no conflicts to disclose.

### Author Contributions

All authors have given approval to the final version of this paper.

**Quadri O. Adewuyi:** Data curation (lead); Formal analysis (equal); Writing – original draft (equal); Writing – review & editing (equal). **Suchona Akter:** Formal analysis (supporting); Writing – review & editing (supporting). **Md Omar Faruque:** Formal analysis (supporting); Writing – review & editing (supporting). **Dil K. Limbu:** Data curation (supporting). **Zhonghua Peng:** Conceptualization (equal); Funding acquisition (equal). **Praveen K. Thallapally:**

Conceptualization (equal); Funding acquisition (equal). **Mohammad R. Momeni:** Conceptualization (equal); Formal analysis (equal); Funding acquisition (equal); Supervision (lead); Writing – original draft (equal); Writing – review & editing (equal).

## DATA AVAILABILITY

The data that support the findings of this study are provided in the main text and the accompanying [supplementary material](#). Additional data are available from the corresponding author upon reasonable request.

## REFERENCES

- <sup>1</sup> M. S. Diallo, M. R. Kotte, and M. Cho, “Mining critical metals and elements from seawater: Opportunities and challenges,” *Environ. Sci. Technol.* **49**, 9390–9399 (2015).
- <sup>2</sup> S. E. Can Sener, V. M. Thomas, D. E. Hogan, R. M. Maier, M. Carbajales-Dale, M. D. Barton, T. Karanfil, J. C. Crittenden, and G. L. Amy, “Recovery of critical metals from aqueous sources,” *ACS Sustainable Chem. Eng.* **9**, 11616–11634 (2021).
- <sup>3</sup> N. R. Kiprono, T. Smolinski, M. Rogowski, and A. G. Chmielewski, “The state of critical and strategic metals recovery and the role of nuclear techniques in the separation technologies development: Review,” *Separations* **10**, 112 (2023).
- <sup>4</sup> P. Loganathan, G. Naidu, and S. Vigneswaran, “Mining valuable minerals from seawater: A critical review,” *Environ. Sci.: Water Res. Technol.* **3**, 37–53 (2017).
- <sup>5</sup> M. G. Buonomenna, “Mining critical metals from seawater by subnanostructured membranes: Is it viable?,” *Symmetry* **14**, 681 (2022).
- <sup>6</sup> B. K. Pramanik, L. D. Nghiem, and F. I. Hai, “Extraction of strategically important elements from brines: Constraints and opportunities,” *Water Res.* **168**, 115149 (2020).
- <sup>7</sup> S. Edebali, *Advanced sorption process applications* (BoD–Books on Demand, 2019).
- <sup>8</sup> S. K. Sikdar, J. Burckle, and J. Rogut, “Separation methods for environmental technologies,” *Environ. Prog.* **20**, 1–11 (2001).
- <sup>9</sup> J. Florek, M. Negoro, Y. Hu, K. Kanamori, K. Nakanishi, and F. Kleitz, “The role of nanoporous adsorbents in the circular economy—Closing the loop of critical materials recovery,” *Adv. Funct. Mater.* **35**, 2409462 (2024).
- <sup>10</sup> S. Iftekhar, G. Heidari, N. Amanat, E. N. Zare, M. B. Asif, M. Hassanpour, V. P. Lehto, and M. Sillanpaa, “Porous materials for the recovery of rare earth elements, platinum group metals, and other valuable metals: A review,” *Environ. Chem. Lett.* **20**, 3697–3746 (2022).
- <sup>11</sup> H. Furukawa, K. E. Cordova, M. O’Keeffe, and O. M. Yaghi, “The chemistry and applications of metal-organic frameworks,” *Science* **341**, 1230444 (2013).
- <sup>12</sup> W. Yang, Q. Pan, S. Song, and H. Zhang, “Metal–organic framework-based materials for the recovery of uranium from aqueous solutions,” *Inorg. Chem. Front.* **6**, 1924–1937 (2019).
- <sup>13</sup> A. P. Cote, A. I. Benin, N. W. Ockwig, M. O’Keeffe, A. J. Matzger, and O. M. Yaghi, “Porous, crystalline, covalent organic frameworks,” *Science* **310**, 1166–1170 (2005).
- <sup>14</sup> S. B. M K, Y.-S. Yun, and S. Kancharla, “Covalent organic frameworks for critical metal recycling from waste,” *Coord. Chem. Rev.* **507**, 215699 (2024).
- <sup>15</sup> W. Guo, J. Liu, H. Tao, J. Meng, J. Yang, Q. Shuai, Y. Asakura, L. Huang, and Y. Yamauchi, “Covalent organic framework nanoarchitectonics: Recent advances for precious metal recovery,” *Adv. Mater.* **36**, 2405399 (2024).
- <sup>16</sup> H. N. Miras, J. Yan, D.-L. Long, and L. Cronin, “Engineering polyoxometalates with emergent properties,” *Chem. Soc. Rev.* **41**, 7403–7430 (2012).
- <sup>17</sup> K. Niinomi, S. Miyazawa, M. Hibino, N. Mizuno, and S. Uchida, “High proton conduction in crystalline composites based on Preyssler-type polyoxometalates and polymers under nonhumidified or humidified conditions,” *Inorg. Chem.* **56**, 15187–15193 (2017).
- <sup>18</sup> S. Uchida, “Frontiers and progress in cation-uptake and exchange chemistry of polyoxometalate-based compounds,” *Chem. Sci.* **10**, 7670–7679 (2019).

- <sup>19</sup>T. Iwano, D. Akutsu, H. Ubukata, N. Ogiwara, Y. Kikukawa, S. Wang, L.-K. Yan, H. Kageyama, and S. Uchida, “Tuning proton conduction by staggered arrays of polar Preyssler-type oxoclusters,” *J. Am. Chem. Soc.* **146**, 26113–26120 (2024).
- <sup>20</sup>C. Dey, “Preyssler-type polyoxometalates, smallest POM with internal cavity: Synthesis, structure and function,” *Coord. Chem. Rev.* **510**, 215847 (2024).
- <sup>21</sup>C. Boskovic, “Rare earth polyoxometalates,” *Acc. Chem. Res.* **50**, 2205–2214 (2017).
- <sup>22</sup>Y. Han, J. Lan, K. Li, L. Yang, C. Zhu, and J. Chen, “The cluster design and redox behavior characterization of polyoxometalates for redox flow batteries,” *Chem.-Asian J.* **17**, e202200950 (2022).
- <sup>23</sup>Y. Lu, Y. Li, E. Wang, X. Xu, and Y. Ma, “A new family of polyoxometalate compounds built up of Preyssler anions and trivalent lanthanide cations,” *Inorg. Chim. Acta* **360**, 2063–2070 (2007).
- <sup>24</sup>M. H. Alizadeh, S. P. Harmalkar, Y. Jeannin, J. Martin-Frere, and M. T. Pope, “A heteropolyanion with fivefold molecular symmetry that contains a nonlabile encapsulated sodium ion. The structure and chemistry of  $[NaP_5W_{30}O_{110}]^{14-}$ ,” *J. Am. Chem. Soc.* **107**, 2662–2669 (1985).
- <sup>25</sup>K.-C. Kim, M. T. Pope, G. J. Gama, and M. H. Dickman, “Slow proton exchange in aqueous solution. Consequences of protonation and hydration within the central cavity of Preyssler anion derivatives,  $[[M(H_2O)\rightrightarrows P_5W_{30}O_{110}]^{n-}]$ ,” *J. Am. Chem. Soc.* **121**, 11164–11170 (1999).
- <sup>26</sup>J. A. Fernández, X. López, C. Bo, C. de Graaf, E. J. Baerends, and J. M. Poblet, “Polyoxometalates with internal cavities: Redox activity, basicity, and cation encapsulation in  $[X^{n+}P_5W_{30}O_{110}]^{(15-n)-}$  Preyssler complexes, with  $X = Ca^+, Ca^{2+}, Y^{3+}, La^{3+}, Ce^{3+}$ , and  $Th^{4+}$ ,” *J. Am. Chem. Soc.* **129**, 12244–12253 (2007).
- <sup>27</sup>A. Hayashi, M. N. K. Wihadi, H. Ota, X. López, K. Ichihashi, S. Nishihara, K. Inoue, N. Tsunogi, T. Sano, and M. Sadakane, “Preparation of Preyssler-type phosphotungstate with one central potassium cation and potassium cation migration into the Preyssler molecule to form Di-potassium-encapsulated derivative,” *ACS Omega* **3**, 2363–2373 (2018).
- <sup>28</sup>A. Hayashi, H. Ota, X. López, N. Hiyoshi, N. Tsunogi, T. Sano, and M. Sadakane, “Encapsulation of two potassium cations in Preyssler-type phosphotungstates: Preparation, structural characterization, thermal stability, activity as an acid catalyst, and HAADF-STEM images,” *Inorg. Chem.* **55**, 11583–11592 (2016).
- <sup>29</sup>M. N. K. Wihadi, A. Hayashi, T. Ozeki, K. Ichihashi, H. Ota, M. Fujibayashi, S. Nishihara, K. Inoue, N. Tsunogi, T. Sano, and M. Sadakane, “Synthesis of Preyssler-type phosphotungstate with sodium cation in the central cavity through migration of the ion,” *Bull. Chem. Soc. Jpn.* **93**, 461–466 (2020).
- <sup>30</sup>I. Creaser, M. C. Heckel, R. J. Neitz, and M. T. Pope, “Rigid nonlabile polyoxometalate cryptates  $[ZP_5W_{30}O_{110}]^{(15-n)-}$  that exhibit unprecedented selectivity for certain lanthanide and other multivalent cations,” *Inorg. Chem.* **32**, 1573–1578 (1993).
- <sup>31</sup>M. R. Antonio and L. Soderholm, “Cerium valence in cerium-exchanged Preyssler’s heteropolyanion through x-ray absorption near-edge structure,” *Inorg. Chem.* **33**, 5988–5993 (1994).
- <sup>32</sup>L. Soderholm, G. K. Liu, J. Muntean, J. Malinsky, and M. R. Antonio, “Coordination and valence of europium in the heteropolyanion  $[EuP_5W_{30}O_{110}]^{12-}$ ,” *J. Phys. Chem.* **99**, 9611–9616 (1995).
- <sup>33</sup>M. R. Antonio and L. Soderholm, “Redox behavior of europium in the Preyssler heteropolyanion  $[EuP_5W_{30}O_{110}]^{12-}$ ,” *J. Clust. Sci.* **7**, 585–591 (1996).
- <sup>34</sup>M. R. Antonio and L. Soderholm, “Implications of the unusual redox behavior exhibited by the heteropolyanion  $[EuP_5W_{30}O_{110}]^{12-}$ ,” *J. Alloys Compd.* **250**, 541–543 (1997).
- <sup>35</sup>M. R. Antonio, L. Soderholm, C. W. Williams *et al.*, “Redox behavior of cerium in heteropolyoxotungstate complexes,” *J. Chem. Soc. Dalton Trans.* **1999**, 3825–3830.
- <sup>36</sup>C. W. Williams, M. R. Antonio, and L. Soderholm, “The formation and stability of  $[EuP_5W_{30}O_{110}]^{12-}$  and  $[AmP_5W_{30}O_{110}]^{12-}$ ,” *J. Alloys Compd.* **303–304**, 509–513 (2000).
- <sup>37</sup>S. Cardona-Serra, J. M. Clemente-Juan, E. Coronado, A. Gaita-Ariño, A. Camón, M. Evangelisti, F. Luis, M. J. Martínez-Pérez, and J. Seée, “Lanthanoid single-ion magnets based on polyoxometalates with a 5-fold symmetry: The series  $[LnP_5W_{30}O_{110}]^{12-}$  ( $Ln^{3+} = Tb, Dy, Ho, Er, Tm$ , and  $Yb$ )”, *J. Am. Chem. Soc.* **134**(36), 14982–14990 (2012).
- <sup>38</sup>K. Takahashi, T. Sano, and M. Sadakane, “Preparation and characterization of Preyssler-type phosphotungstic acid,  $H_{15-n}[P_5W_{30}O_{110}M^{n+}]$ , with different encapsulated cations ( $M = Na, Ca, Bi, Eu, Y$ , or  $Ce$ ), and their thermal stability and acid catalyst properties,” *Z. Anorg. Allg. Chem.* **640**, 1314–1321 (2014).
- <sup>39</sup>Y.-Q. Zhao, K. Yu, L.-W. Wang, Y. Wang, X.-P. Wang, and D. Sun, “Anion-induced supramolecular isomerism in two Preyssler  $P_5W_{30}$  polyoxometalate-based hybrid materials,” *Inorg. Chem.* **53**, 11046–11050 (2014).
- <sup>40</sup>T.-P. Hu, Y.-Q. Zhao, Z. Jagličić, K. Yu, X.-P. Wang, and D. Sun, “Four hybrid materials based on Preyssler  $P_5W_{30}$  polyoxometalate and first-row transition-metal complex,” *Inorg. Chem.* **54**, 7415–7423 (2015).
- <sup>41</sup>M.-X. Liang, C.-Z. Ruan, D. Sun, X.-J. Kong, Y.-P. Ren, L.-S. Long, R.-B. Huang, and L.-S. Zheng, “Solvothermal synthesis of four polyoxometalate-based coordination polymers including diverse  $Ag(I) \dots \pi$  interactions,” *Inorg. Chem.* **53**, 897–902 (2014).
- <sup>42</sup>J. Du, M.-D. Cao, S.-L. Feng, F. Su, X.-J. Sang, L.-C. Zhang, W.-S. You, M. Yang, and Z.-M. Zhu, “Two new Preyssler-type polyoxometalate-based coordination polymers and their application in horseradish peroxidase immobilization,” *Chem.-Eur. J.* **23**, 14614–14622 (2017).
- <sup>43</sup>C. Kato, K. Y. Maryunina, K. Inoue, S. Yamaguchi, H. Miyaoka, A. Hayashi, M. Sadakane, R. Tsunashima, and S. Nishihara, “Synthesis, characterization, and structure of a reduced Preyssler-type polyoxometalate,” *Chem. Lett.* **46**, 602–604 (2017).
- <sup>44</sup>M. H. Dickman, G. J. Gama, K.-C. Kim, and M. T. Pope, “The structures of europium (III)-and uranium (IV) derivatives of  $[P^5W^{30}O^{110}]_{15-}$ : Evidence for ‘cryptohydration’,” *J. Clust. Sci.* **7**, 567–583 (1996).
- <sup>45</sup>C. M. Granadeiro, B. de Castro, S. S. Balula, and L. Cunha-Silva, “Lanthanopolyoxometalates: From the structure of polyanions to the design of functional materials,” *Polyhedron* **52**, 10–24 (2013).
- <sup>46</sup>A. Hayashi, T. Haioka, K. Takahashi, B. S. Basil, U. Kortz, T. Sano, and M. Sadakane, “Cation effect on formation of Preyssler-type 30-tungsto-5-phosphate: Enhanced yield of Na-encapsulated derivative and direct synthesis of Ca- and Bi-encapsulated derivatives,” *Z. Anorg. Allg. Chem.* **641**, 2670–2676 (2015).
- <sup>47</sup>M. R. Antonio and M.-H. Chiang, “Stabilization of Plutonium(III) in the Preyssler polyoxometalate,” *Inorg. Chem.* **47**, 8278–8285 (2008).
- <sup>48</sup>Y. Zhang, Y. Liu, D. Wang, J. Liu, J. Zhao, and L. Chen, “State-of-the-art advances in the syntheses, structures, and applications of polyoxometalate-based metal–organic frameworks,” *Polyoxometalates* **2**, 9140017 (2023).
- <sup>49</sup>S. Zhang, F. Ou, S. Ning, and P. Cheng, “Polyoxometalate-based metal–organic frameworks for heterogeneous catalysis,” *Inorg. Chem. Front.* **8**, 1865–1899 (2021).
- <sup>50</sup>H. N. Miras, L. Vilà-Nadal, and L. Cronin, “Polyoxometalate based open-frameworks (POM-OFs),” *Chem. Soc. Rev.* **43**, 5679–5699 (2014).
- <sup>51</sup>C. Streb, “New trends in polyoxometalate photoredox chemistry: From photosensitisation to water oxidation catalysis,” *Dalton Trans.* **41**, 1651 (2012).
- <sup>52</sup>A. Dolbecq, E. Dumas, C. R. Mayer, and P. Mialane, “Hybrid organic–inorganic polyoxometalate compounds: From structural diversity to applications,” *Chem. Rev.* **110**, 6009–6048 (2010).
- <sup>53</sup>M. H. Alizadeh, H. Razavi, F. Farrash Bamoharram, M. K. Hassanzadeh, R. Khoshnavaz, and F. Mohammadi Zonoz, “Novel catalytic acetylation of alcohols with Preyssler’s anion,  $[NaP_5W_{30}O_{110}]^{14-1}$ ,” *Kinet. Catal.* **44**, 524–528 (2003).
- <sup>54</sup>I. Batatia, D. P. Kovacs, G. Simm, C. Ortner, and G. Csányi, “MACE: Higher order equivariant message passing neural networks for fast and accurate force fields,” *Adv. Neural Inf. Process. Syst.* **35**, 11423–11436 (2022).
- <sup>55</sup>I. Batatia, P. Benner, Y. Chiang, A. M. Elena, D. P. Kovács, J. Riebesell, X. R. Advincula, M. Asta, M. Avaylon, W. J. Baldwin *et al.*, “A foundation model for atomistic materials chemistry,” *arXiv:2401.00096* (2023).
- <sup>56</sup>P. H. Hünenberger and W. F. van Gunsteren, “Empirical classical force fields for molecular systems,” in *Potential Energy Surfaces: Proceedings of the Mariaparr Workshop in Theoretical Chemistry* (Springer, 1999), pp. 177–214.
- <sup>57</sup>S. Amira, D. Spångberg, V. Zelin, M. Probst, and K. Hermansson, “Car–Parrinello molecular dynamics simulation of  $Fe^{3+}$  (aq),” *J. Phys. Chem. B* **109**, 14235–14242 (2005).
- <sup>58</sup>E. C. Beret, J. M. Martinez, R. R. Pappalardo, E. S. Marcos, N. L. Dotsiris, and D. Marx, “Explaining asymmetric solvation of Pt (II) versus Pd (II) in aqueous solution revealed by ab initio molecular dynamics simulations,” *J. Chem. Theory Comput.* **4**, 2108–2121 (2008).
- <sup>59</sup>T. P. Senftle, S. Hong, M. M. Islam, S. B. Kyela, Y. Zheng, Y. K. Shin, C. Junkermeier, R. Engel-Herbert, M. J. Janik, H. M. Aktulgul *et al.*, “The ReaxFF reactive

- force-field: Development, applications and future directions," *npj Comput. Mater.* **2**, 15011 (2016).
- <sup>60</sup>P. Dauber-Osguthorpe and A. T. Hagler, "Biomolecular force fields: Where have we been, where are we now, where do we need to go and how do we get there?," *J. Comput. Aided Mol. Des.* **33**, 133–203 (2019).
- <sup>61</sup>L. Bonati and M. Parrinello, "Silicon liquid structure and crystal nucleation from *ab initio* deep Metddynamics," *Phys. Rev. Lett.* **121**, 265701 (2018).
- <sup>62</sup>L. Zhao, H. Zong, X. Ding, J. Sun, and G. J. Ackland, "Commensurate-incommensurate phase transition of dense potassium simulated by machine-learned interatomic potential," *Phys. Rev. B* **100**, 220101 (2019).
- <sup>63</sup>H. Niu, L. Bonati, P. M. Piaggi, and M. Parrinello, "Ab initio phase diagram and nucleation of gallium," *Nat. Commun.* **11**, 2654 (2020).
- <sup>64</sup>D. P. Kovács, J. H. Moore, N. J. Browning, I. Batatia, J. T. Horton, Y. Pu, V. Kapil, W. C. Witt, I.-B. Magdau, D. J. Cole et al., "MACE-OFF: Short-range transferable machine learning force fields for organic molecules," *J. Am. Chem. Soc.* **147**(21), 17598–17611 (2025).
- <sup>65</sup>D. P. Kovács, J. H. Moore, N. J. Browning, I. Batatia, J. T. Horton, V. Kapil, W. C. Witt, I.-B. Magdau, D. J. Cole, and G. Csányi, "MACE-OFF23: Transferable machine learning force fields for organic molecules," *Journal of the American Chemical Society* **147**(21), 17598–17611 (2025).
- <sup>66</sup>I. Y. Chernyshov and E. A. Pidko, "MACE: Automated assessment of stereochemistry of transition metal complexes and its applications in computational catalysis," *J. Chem. Theory Comput.* **20**, 2313–2320 (2024).
- <sup>67</sup>E. Gelžinytė, M. Ören, M. D. Segall, and G. Csányi, "Transferable machine learning interatomic potential for bond dissociation energy prediction of drug-like molecules," *J. Chem. Theory Comput.* **20**, 164–177 (2023).
- <sup>68</sup>S. G. Brookes, V. Kapil, A. Michaelides, and C. Schran, "CO<sub>2</sub> hydration at the air-water interface: A surface-mediated 'in and out' mechanism," *arXiv:2502.08348* (2025).
- <sup>69</sup>J. Behler, "Perspective: Machine learning potentials for atomistic simulations," *J. Chem. Phys.* **145**, 170901 (2016).
- <sup>70</sup>K. T. Butler, D. W. Davies, H. Cartwright, O. Isayev, and A. Walsh, "Machine learning for molecular and materials science," *Nature* **559**, 547–555 (2018).
- <sup>71</sup>V. L. Deringer, M. A. Caro, and G. Csányi, "Machine learning interatomic potentials as emerging tools for materials science," *Adv. Mater.* **31**, 1902765 (2019).
- <sup>72</sup>P.-L. Kang, C. Shang, and Z.-P. Liu, "Large-scale atomic simulation via machine learning potentials constructed by global potential energy surface exploration," *Acc. Chem. Res.* **53**, 2119–2129 (2020).
- <sup>73</sup>Y. Mishin, "Machine-learning interatomic potentials for materials science," *Acta Mater.* **214**, 116980 (2021).
- <sup>74</sup>J. Behler, "Four generations of high-dimensional neural network potentials," *Chem. Rev.* **121**, 10037–10072 (2021).
- <sup>75</sup>C. Schran, F. L. Thiemann, P. Rowe, E. A. Müller, O. Marsalek, and A. Michaelides, "Machine learning potentials for complex aqueous systems made simple," *Proc. Natl. Acad. Sci. U. S. A.* **118**, e2110077118 (2021).
- <sup>76</sup>L. Martínez, R. Andrade, E. G. Birgin, and J. M. Martínez, "PACKMOL: A package for building initial configurations for molecular dynamics simulations," *J. Comput. Chem.* **30**, 2157–2164 (2009).
- <sup>77</sup>J. P. Perdew, K. Burke, and M. Ernzerhof, "Generalized gradient approximation made simple," *Phys. Rev. Lett.* **77**, 3865 (1996).
- <sup>78</sup>J. VandeVondele, M. Krack, F. Mohamed, M. Parrinello, T. Chassaing, and J. Hutter, "Quickstep: Fast and accurate density functional calculations using a mixed Gaussian and plane waves approach," *Comput. Phys. Commun.* **167**, 103–128 (2005).
- <sup>79</sup>J. Hutter, M. Iannuzzi, F. Schiffmann, and J. VandeVondele, "cp2k: atomistic simulations of condensed matter systems," *WIREs Comput. Mol. Sci.* **4**, 15–25 (2014).
- <sup>80</sup>S. Grimme, J. Antony, S. Ehrlich, and H. Krieg, "A consistent and accurate *ab initio* parametrization of density functional dispersion correction (DFT-D) for the 94 elements H-Pu," *J. Chem. Phys.* **132**, 154104 (2010).
- <sup>81</sup>S. Grimme, S. Ehrlich, and L. Goerigk, "Effect of the damping function in dispersion corrected density functional theory," *J. Comput. Chem.* **32**, 1456–1465 (2011).
- <sup>82</sup>S. Goedecker, M. Teter, and J. Hutter, "Separable dual-space Gaussian pseudopotentials," *Phys. Rev. B* **54**, 1703 (1996).
- <sup>83</sup>G. C. Moore, M. K. Horton, E. Linscott, A. M. Ganose, M. Siron, D. D. O'Regan, and K. A. Persson, "High-throughput determination of Hubbard *U* and Hund *J* values for transition metal oxides via the linear response formalism," *Phys. Rev. Mater.* **8**, 014409 (2024).
- <sup>84</sup>G. Bussi, D. Donadio, and M. Parrinello, "Canonical sampling through velocity rescaling," *J. Chem. Phys.* **126**, 014101 (2007).
- <sup>85</sup>A. H. Larsen, J. J. Mortensen, J. Blomqvist, I. E. Castelli, R. Christensen, M. Dufak, J. Friis, M. N. Groves, B. Hammer, C. Hargus et al., "The atomic simulation environment—A Python library for working with atoms," *J. Phys.: Condens. Matter* **29**, 273002 (2017).
- <sup>86</sup>A. Laio and M. Parrinello, "Escaping free-energy minima," *Proc. Natl. Acad. Sci. U. S. A.* **99**, 12562–12566 (2002).
- <sup>87</sup>O. Valsson, P. Tiwary, and M. Parrinello, "Enhancing important fluctuations: Rare events and metadynamics from a conceptual viewpoint," *Annu. Rev. Phys. Chem.* **67**, 159–184 (2016).
- <sup>88</sup>G. Bussi and A. Laio, "Using metadynamics to explore complex free-energy landscapes," *Nat. Rev. Phys.* **2**, 200–212 (2020).
- <sup>89</sup>M. Yang, L. Bonati, D. Polino, and M. Parrinello, "Using metadynamics to build neural network potentials for reactive events: the case of urea decomposition in water," *Catal. Today* **387**, 143–149 (2022).
- <sup>90</sup>P. Raiteri, A. Laio, F. L. Gervasio, C. Micheletti, and M. Parrinello, "Efficient reconstruction of complex free energy landscapes by multiple walkers metadynamics," *J. Phys. Chem. B* **110**, 3533–3539 (2006).
- <sup>91</sup>A. Barducci, G. Bussi, and M. Parrinello, "Well-tempered metadynamics: A smoothly converging and tunable free-energy method," *Phys. Rev. Lett.* **100**, 020603 (2008).
- <sup>92</sup>J. F. Dama, M. Parrinello, and G. A. Voth, "Well-tempered metadynamics converges asymptotically," *Phys. Rev. Lett.* **112**, 240602 (2014).
- <sup>93</sup>M. Invernizzi and M. Parrinello, "Exploration vs convergence speed in adaptive-bias enhanced sampling," *J. Chem. Theory Comput.* **18**, 3988–3996 (2022).
- <sup>94</sup>P. Hošek, P. Kříž, D. Toulcová, and V. Spiwok, "Multisystem altruistic metadynamics—Well-tempered variant," *J. Chem. Phys.* **146**, 125103 (2017).
- <sup>95</sup>Y. Xie and S. Calabrese Barton, "Infrequent metadynamics study of rare-event electrostatic channeling," *Phys. Chem. Chem. Phys.* **23**, 13381–13388 (2021).
- <sup>96</sup>G. A. Tribello, M. Bonomi, D. Branduardi, C. Camilloni, and G. Bussi, "PLUMED 2: New feathers for an old bird," *Comput. Phys. Commun.* **185**, 604–613 (2014).
- <sup>97</sup>G. A. Tribello, M. Bonomi, G. Bussi, C. Camilloni, B. I. Armstrong, A. Arsiccio, S. Aureli, F. Ballabio, M. Bernetti, L. Bonati et al., "PLUMED Tutorials: A collaborative, community-driven learning ecosystem," *J. Chem. Phys.* **162**(9), 092501 (2025).
- <sup>98</sup>M. Miklitz and K. E. Jelfs, "pywindow: Automated structural analysis of molecular pores," *J. Chem. Inf. Model.* **58**, 2387–2391 (2018).
- <sup>99</sup>X. López, C. Nieto-Draghi, C. Bo, J. B. Avalos, and J. M. Poblet, "Polyoxometalates in solution: Molecular dynamics simulations on the  $\alpha$ -PW<sub>12</sub>O<sub>40</sub><sup>3-</sup> keggin anion in aqueous media," *J. Phys. Chem. A* **109**, 1216–1222 (2005).
- <sup>100</sup>T. J. Boerner, S. Deems, T. R. Furlani, S. L. Knuth, and J. Towns, "ACCESS: Advancing innovation: NSF's advanced cyberinfrastructure coordination ecosystem: Services & support," in *Practice and Experience in Advanced Research Computing, PEARC '23* (Association for Computing Machinery, New York, NY, 2023), pp. 173–176.